Geochemical Perspectives Letters

Co-reduction of Fe(III) and S^0 drives Fe-S biomineral formation and phosphate mobilisation

R. Bronner[1#], K. Thompson[2#], C. Dreher[1], E. Runge[3], E. Voggenreiter[1], J. Shuster[4], B. Wan[1], P. Joshi[1], S. Fischer[4], J.-P. Duda[3], A. Kappler[1,5], M. Mansor[1*]

OPEN ACCESS

https://doi.org/10.7185/geochemlet.2301

Abstract

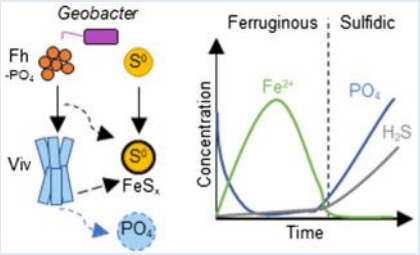

Microbially mediated iron and sulfur cycling have impacted redox transitions and the bioavailability of nutrients throughout Earth's history. Here, we incubated *Geobacter sulfurreducens* in the co-presence of ferrihydrite and S^0 at pH 6.5, 7.2 or 8.0. Microbial reduction of Fe(III) and S^0 resulted in a shift from ferruginous (Fe^{2+}-rich) to sulfidic (sulfide-rich) conditions and the precipitation of mackinawite, greigite and vivianite. The initial pH controlled the timing of the ferruginous-sulfidic transition and the relative abundance and crystallinity of the formed minerals. Vivianite formation was attributed to phosphate initially added to the medium. Phosphate showed a dynamic cycle, with low dissolved concentrations initially due to sorption to ferrihydrite, followed by vivianite precipitation under ferruginous conditions, and a significant release under sulfidic conditions. Co-reduction of Fe(III) and S^0 therefore regulates Fe-S biomineral formation and P bioavailability, which could be particularly important to consider in microbial mats and the sulfate-poor Archean ocean.

Received 15 September 2022 | Accepted 12 December 2022 | Published 17 January 2023

Introduction

Microbially mediated Fe and S cycling are vital parts of Earth's history that affected the oceanic transition between ferruginous and sulfidic conditions, as well as playing an integral role in modern biogeochemical cycles of greenhouse gases, nutrients and contaminants (Lepot, 2020; Kappler *et al.*, 2021). Many species, including model organisms *Geobacter* and *Shewanella*, are capable of linking the Fe and S cycles through the reduction of Fe(III) minerals and elemental sulfur (S^0). This metabolic flexibility enables them to survive under alkaline conditions when Fe(III) reduction becomes thermodynamically unfeasible (Flynn *et al.*, 2014), resulting in Fe sulfide biomineral formation (Wang *et al.*, 2018; Nie *et al.*, 2020; Ye and Jing, 2022; Liu *et al.*, 2023). Investigations of coupled reduction of Fe(III) and S^0 are important for mineral biosignatures and their impact on nutrient bioavailability, especially in environments where S^0 could be an important electron acceptor such as in microbial mats and sulfate-poor Archean oceans (Troelsen and Jørgensen, 1982; van Gemerden *et al.*, 1989; Philippot *et al.*, 2007; Galić *et al.*, 2017). The mobilisation and bioavailability of phosphate in particular is affected by Fe and S biogeochemistry with direct consequences to primary productivity, climate and Earth's redox evolution (Alcott *et al.*, 2022).

Microbial Metabolism Drives Geochemical Shifts

To investigate biomineral formation during co-reduction of Fe(III) and S^0, *G. sulfurreducens* was incubated in the co-presence of ferrihydrite (30 mM) and S^0 (60 mM) with acetate as excess electron donor. Different initial pH values (6.5, 7.2 or 8.0) were employed. Over 42 days of incubation, all cultures exhibited a colour change from dark brown to black, indicating transformation of ferrihydrite to reduced Fe minerals (Fig. S-1). From initial pH values of 6.5 and 7.2, pH increased to 7.1 and 7.5, respectively. At initial pH of 8.0, the pH slightly decreased to 7.9. From here onward, the cultures will be referred to by their initial pH values for simplicity.

At the beginning, solid phase extractable Fe (6 M HCl) amounted to 29.1 ± 2.2 mM ($n = 12$) with no Fe(II) components detected. Within 15 days, the Fe(II)/Fe(III) percentages of the HCl extractable Fe approached 100 %, indicating Fe(III) reduction (Fig. S-2). Note that the total HCl extractable Fe decreased over time, and we attributed this primarily to sampling inhomogeneity due to mineral aggregation. Fe(III) reduction was accompanied by the release of Fe^{2+} into solution, reaching maxima of 1000–2000 µM depending on initial pH (Fig. 1). Dissolved Fe^{2+} showed a decline to <500 µM within 12 days after the maximum. Once Fe^{2+} reached low levels, dissolved sulfide started to

1. Geomicrobiology, Center for Applied Geosciences, University of Tuebingen, 72076 Tuebingen, Germany
2. Microbial Ecology, Center for Applied Geosciences, University of Tuebingen, 72076 Tuebingen, Germany
3. Sedimentology and Organic Geochemistry, Center for Applied Geosciences, University of Tuebingen, 72076 Tuebingen, Germany
4. Tuebingen Structural Microscopy Core Facility, University of Tuebingen, 72076 Tuebingen, Germany
5. Cluster of Excellence: EXC 2124: Controlling Microbes to Fight Infection, Tuebingen, Germany

Co-first authors
* Corresponding author (email: muammar.muammar-bin-mansor@uni-tuebingen.de)

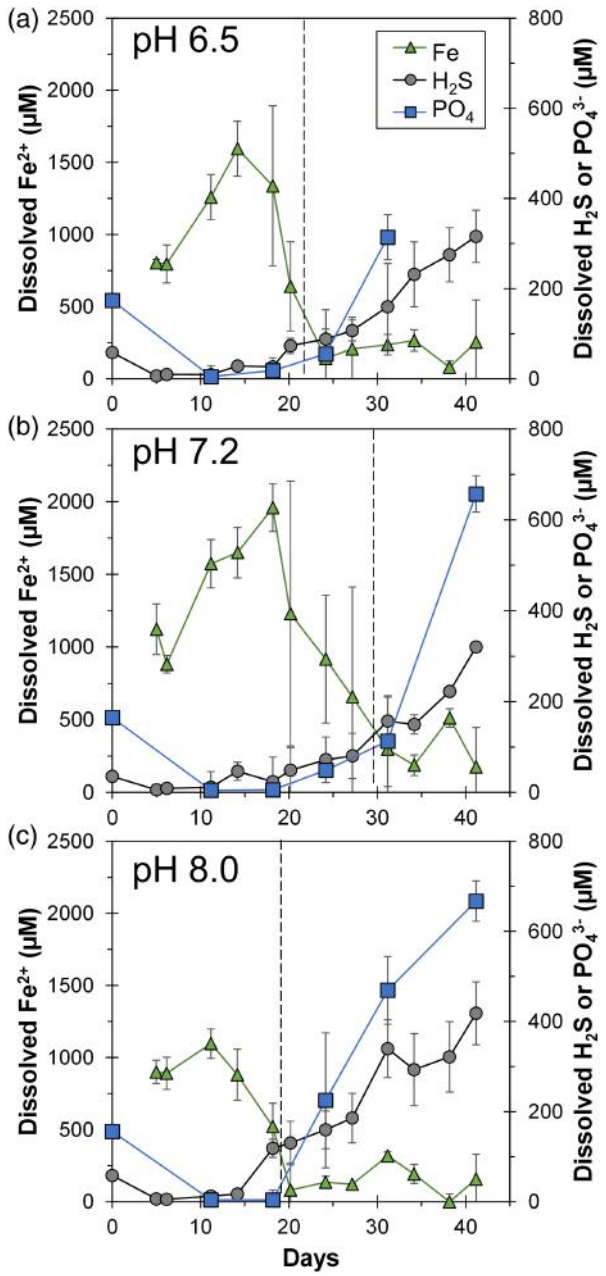

Figure 1 Geochemical evolution of dissolved Fe^{2+}, total sulfide and phosphate at **(a)** pH 6.5, **(b)** pH 7.2, and **(c)** pH 8.0. Dashed vertical lines denote the shift from ferruginous to sulfidic conditions.

increase, reaching maxima of 320–420 μM. Solid phase Fe sulfides were not quantified but were detectable by scanning electron microscopy (SEM), X-ray diffraction (XRD) and Mössbauer spectroscopy (Figs. 2, 3).

Overall, cultures at different pH values exhibited similar geochemical trends with differences in timing and the amount of Fe^{2+} and sulfide released to the solution. Parallel abiotic controls showed neither Fe(II) nor sulfide production (Fig. S-2). The geochemical evolution can be divided into two stages. In the first stage, *ferruginous conditions* dominated as ferrihydrite was reduced and Fe^{2+} accumulated in solution. In the second stage, *sulfidic conditions* were observed once reactive Fe(III) surfaces were exhausted and sulfide accumulated in solution. The time at which the shift from ferruginous to sulfidic conditions occurred differed depending on the pH values, following the order: pH 7.2 (30 days) > pH 6.5 (22 days) > pH 8.0 (19 days). Mirroring this trend, the highest maximum Fe^{2+} followed the order: pH 7.2 (2000 μM) > pH 6.5 (1500 μM) > pH 8.0 (1100 μM). Maximum dissolved sulfide followed the opposite trend: pH 7.2 ≈ pH 6.5 (320 μM) < pH 8.0 (420 μM).

The different timings and concentrations of Fe^{2+} and sulfide observed depend on a number of interrelated pH dependent processes including microbial preference of Fe(III) over S^0, Fe^{2+} adsorption to ferrihydrite, sulfide mediated ferrihydrite reduction and Fe mineral precipitation. These processes can lead to secondary phenomena such as Fe^{2+} catalysed recrystallisation, decreased reactivity from the FeS surface coating, and formation of polysulfides (Peiffer *et al.*, 2015). Notably, the observed geochemical trends do not follow straightforward predictions based on initial pH (Supplementary Information). Further extensive investigation at the nanometre (*e.g.*, transmission electron microscopy) and molecular (*e.g.*, speciation *via* synchrotron) scales, coupled to a biogeochemical model will be needed to elucidate the specific mechanisms.

Formation of Biogenic Mackinawite and Greigite, but not Pyrite

Mineral products were identified using a combination of magnetic testing, XRD, SEM and Mössbauer spectroscopy. XRD patterns of samples at day 21 and 42 indicated the presence of S^0, which decreased over time at all pH values, signifying continuous microbial S^0 reduction (Fig. 3a). Additionally, XRD and Mössbauer identified mackinawite (FeS) as a major product (20–70 % of solid phase Fe). Black colourations typical of Fe sulfides were commonly observed to form coatings on S^0 (Fig. 2c, d).

We report the first instance of greigite (Fe_3S_4) formation by *Geobacter*. The presence of a magnetic mineral was first suggested *via* attraction of the minerals to a hand magnet held next to the bottles. Strong magnetism was observed at all pH values starting from day 11 (Fig. S-1) but decreased noticeably after 27 days (Supplementary Information). Greigite was identified by Mössbauer spectroscopy, making up 17–53 % of solid phase Fe with the highest percentage at pH 7.2. XRD data showed clear patterns for greigite only at pH 6.5 at day 21. Positive identification in other cultures was complicated due to the overlap of the main greigite signal with mackinawite at ~35° 2θ and the generally broad patterns resulting from low crystallinity. Consistent with this interpretation, crystalline greigite particles were not observed by SEM. Other minerals such as magnetite (Fe_3O_4) and pyrite were not detectable within 21–42 days of incubation (Supplementary Information).

The mechanism and kinetics of biogenic Fe sulfide mineral transformation are important to understand with respect to their implications for biosignatures and elemental cycling (Picard *et al.*, 2016; Nie *et al.*, 2020). Poorly-crystalline mackinawite typically forms first from the reaction between Fe^{2+} and sulfide at low temperatures, followed by its transformation to greigite and pyrite over time (Son *et al.*, 2022). In our cultures, the XRD patterns for mackinawite were most pronounced at pH 7.2, and inspection of the main signal at ~18° 2θ showed that it became broader over time at all pH values, suggesting an overall decrease in bulk crystallinity. This can be understood in terms of different populations of mackinawite that formed under ferruginous *versus* sulfidic conditions. Mackinawite formed in excess Fe (ferruginous conditions) tends to exhibit higher crystallinity and sharper diffraction patterns than that formed in excess S (sulfidic conditions) (Bourdoiseau *et al.*, 2008). This is consistent with the timing of the stages in our cultures. The pH 7.2 cultures had the longest ferruginous stage that encompassed the period at which the first XRD samples were collected (21 days); therefore,

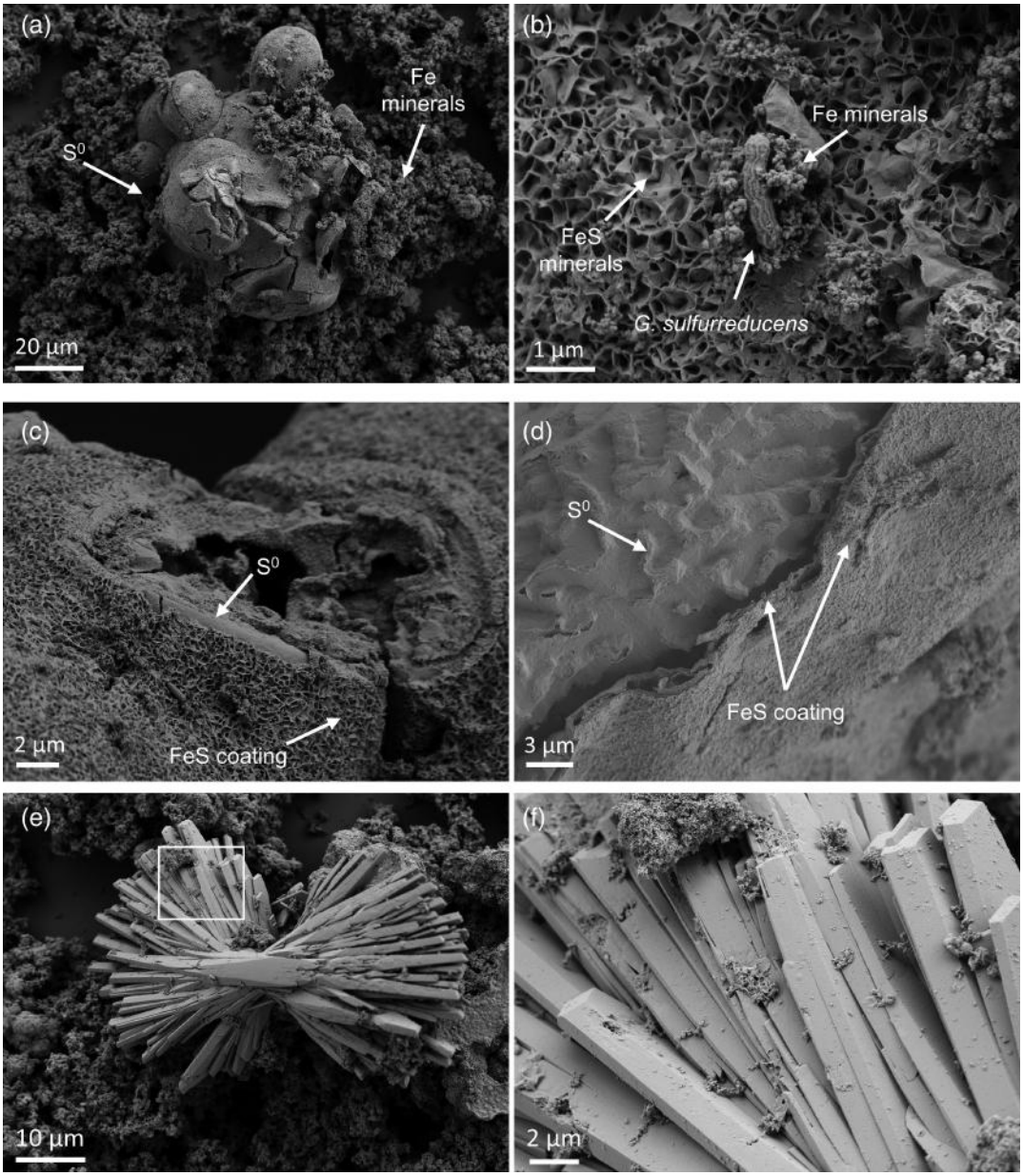

Figure 2 SEM micrographs of microbe-mineral associations. **(a)** S^0 aggregates consisting of ~20 µm globules and Fe mineral aggregates consisting of nanometre-sized structures. **(b)** *G. sulfurreducens* atop a S^0 globule. Note the close spatial association with aggregates of Fe-O minerals and FeS-rich minerals with pseudo-honeycomb structure. **(c)** A naturally fractured sample highlighting the FeS-rich coating on a S^0 globule. **(d)** The FeS-rich coating appeared to peel off, revealing the smoother surface texture of S^0 compared to FeS. **(e)** Typical morphology of Fe-P-O-rich minerals (vivianite). **(f)** A higher magnification of the radial blade-like morphology of vivianite (from the boxed region in **(e)**).

crystalline mackinawite is expected. With longer incubation, the cultures shifted to sulfidic conditions, promoting additional mackinawite formation. However, this mackinawite exhibited lower crystallinity and contributed to broader XRD patterns reflective of the bulk mixture.

Greigite is increasingly recognised as a common and stable phase in nature and as an important intermediate for pyrite formation (Subramani *et al.*, 2020). We found the highest percentage of greigite at the intermediate pH of 7.2 (53 % of solid phase Fe). This is in contrast with the expectation that lower pH, including around the microenvironments of sulfate reducing bacteria, could promote mackinawite's transformation to greigite (Bourdoiseau *et al.*, 2011; Mansor *et al.*, 2019). Instead of pH, we suggest that the crystallinity of the precursor mackinawite is the main controlling factor of transformation kinetics (Csákberényi-Malasics *et al.*, 2012; Miller *et al.*, 2020). As discussed, we observed mackinawite with the highest crystallinity at pH 7.2. Our data showed that precipitation under ferruginous conditions enhances mackinawite's crystallinity and its transformation to greigite, confirming recent predictions from density functional theory (Son *et al.*, 2022).

Pyrite, the most common Fe sulfide mineral in the environment, was not formed in our cultures within 42 days, similar to in pure cultures of sulfate reducing bacteria (Picard *et al.*, 2016). Nonetheless, studies with sulfur cycling bacteria have demonstrated pyrite formation from sulfidation of Fe(III) phosphates within one month (Berg *et al.*, 2020; Duverger *et al.*, 2020). Pyrite precipitation was attributed to microbial production of

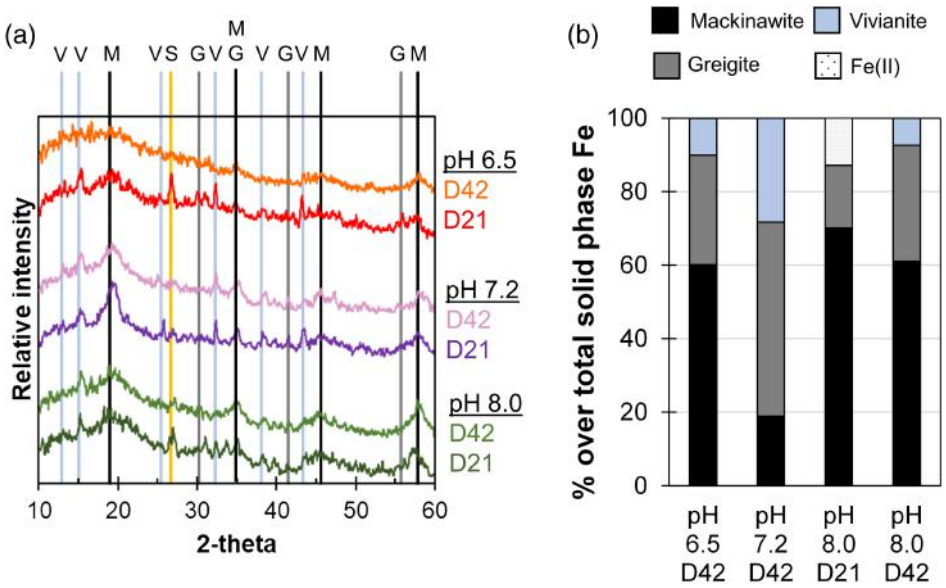

Figure 3 **(a)** XRD patterns of precipitates at Days (D) 21 and 42. Vertical lines denote 2θ positions specific to certain minerals, with colours corresponding to vivianite ('V', light blue), mackinawite ('M', black), S^0 ('S', yellow) and greigite ('G', grey). **(b)** Solid phase Fe distribution based on Mössbauer spectroscopy at 77 K.

extracellular polymeric substances (EPS) that concentrated key ingredients for pyrite formation locally and the continuous formation of Fe^{2+}, S^0 and polysulfides from slow sulfide mediated Fe(III) dissolution. *G. sulfurreducens* is also known to produce EPS that can bind cations, especially in the presence of Fe(III) minerals (Stöckl *et al.*, 2019; Tomaszewski *et al.*, 2020). Furthermore, the co-presence of Fe(III) and S^0 should have led to high polysulfide concentrations that enhance pyrite formation. However, it is possible that rapid reduction of Fe(III) and S^0 (and potentially polysulfides) by *G. sulfurreducens* may have prevented the accumulation of intermediates necessary for fast pyrite formation. Further kinetic based studies and comparison with a pyrite forming culture will be necessary to elucidate factors controlling pyrite formation (Supplementary Information).

Microbial Fe-S Metabolism leads to Phosphate (Im)Mobilisation

Besides Fe sulfides, XRD and Mössbauer spectroscopy revealed the presence of vivianite [$Fe_3(PO_4)_2 \cdot 8\ H_2O$] at all pH values, making up 7–28 % of solid phase Fe (Fig. 3). The formed vivianite had radial blade-like structures up to 50 µm in length (Fig. 2e, f). Vivianite formation is explained by the addition of phosphate to the medium, which resulted in P/Fe ratio of 0.15 in our experiments, comparable to the ~0.10 ratio typical in nature (Kraal *et al.*, 2022).

Despite the addition of 4.4 mM phosphate, initial dissolved phosphate was <200 µM (Fig. 1). We attributed this to strong phosphate adsorption to ferrihydrite (Wang *et al.*, 2013; Kraal *et al.*, 2022). The concentrations dropped within a few days to near detection limit, coincident with the rise in Fe^{2+}, attributed to vivianite formation. Dissolved phosphate then showed a marked increase coincident with sulfide release to solution.

The sequence of biogeochemical processes in the experiments can be summarised as follows (Fig. 4). First, phosphate from the growth medium was rapidly adsorbed to ferrihydrite. *G. sulfurreducens* reduced ferrihydrite and S^0 in the presence of excess electron donor, with more S^0 reduction at pH 8.0 compared to lower pH values. In the early ferruginous stage, sulfide concentration was kept low as it reacted rapidly with ferrihydrite, contributing to Fe(III) reduction, Fe^{2+} release to solution, and the precipitation of mackinawite, greigite and vivianite. The cultures progressed into the late sulfidic stage as reactive Fe(III) became fully exhausted. In addition to further Fe sulfide formation, this biogeochemical switch resulted in vivianite dissolution, releasing phosphate into solution. This supports previous observations in which the switch from ferruginous to sulfidic conditions has been recognised to increase the bioavailability of phosphate (Duverger *et al.*, 2020; Alcott *et al.*, 2022).

Overall, our study demonstrated that co-reduction of Fe(III) and S^0 leads to formation of mackinawite, greigite and vivianite, but not pyrite within 42 days. Initial pH affected the length and timing of the ferruginous-sulfide transition, resulting in differences in the crystallinity and relative abundance of the mineral products. The transition from ferruginous to sulfidic

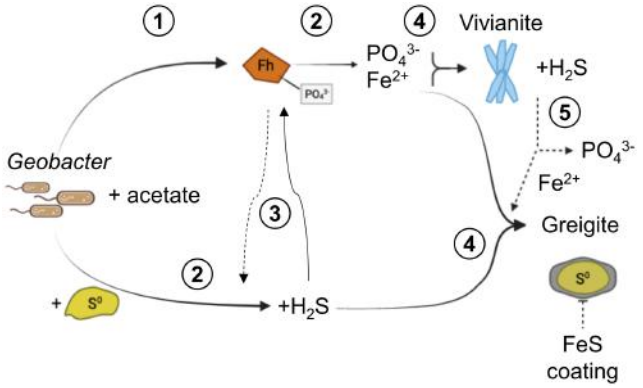

Figure 4 Summary of biogeochemical processes in the cultures. (1) Adsorption of phosphate from growth medium onto ferrihydrite (Fh). (2) Concurrent reduction of Fh and S^0 by *G. sulfurreducens*. (3) Sulfide mediated reduction of Fh. (4) Precipitation of vivianite, mackinawite and greigite. (5) Dissolution of vivianite by H_2S, releasing phosphate into solution.

conditions was associated with phosphate release. Similar processes, driven by the activity of whole microbial communities instead of a single species, are likely important to consider for micro-niches in modern sediments and microbial mats. These processes are further applicable to SO_4-poor Archean oceans and ultimately the investigation of Fe-S biomineral signatures and the bioavailability of important nutrients that affected primary productivity and Earth's biogeochemical evolution.

Acknowledgements

This study was supported by the DFG (SPP 1833, Emmy Noether Programme, 1450/3-1, DU 1450/3-2, DU 1450/7-1, JPD; INST 37/1027-1 FUGG, AK) as well as the Excellence Strategy of the German Federal and State Governments (EXC2124, 390838134; Tuebingen Structural Microscopy Core Facility; AK, MM, PJ, SF, JS). We thank Prof. D.J. Lunter and Yali Liu for assistance with Raman analysis.

Editor: Juan Liu

Additional Information

Supplementary Information accompanies this letter at https://www.geochemicalperspectivesletters.org/article2301.

Cite this letter as: Bronner, R., Thompson, K., Dreher, C., Runge, E., Voggenreiter, E., Shuster, J., Wan, B., Joshi, P., Fischer, S., Duda, J.-P., Kappler, A., Mansor, M. (2023) Co-reduction of Fe(III) and S^0 drives Fe-S biomineral formation and phosphate mobilisation. *Geochem. Persp. Let.* 24, 27–32. https://doi.org/10.7185/geochemlet.2301

References

Alcott, L.J., Mills, B.J.W., Bekker, A., Poulton, S.W. (2022) Earth's Great Oxidation Event facilitated by the rise of sedimentary phosphorus recycling. *Nature Geoscience* 15, 210–215. https://doi.org/10.1038/s41561-022-00906-5

Berg, J.S., Duverger, A., Cordier, L., Laberty-Robert, C., Guyot, F., Miot, J. (2020) Rapid pyritization in the presence of a sulfur/sulfate-reducing bacterial consortium. *Scientific Reports* 10, 8264. https://doi.org/10.1038/s41598-020-64990-6

Bourdoiseau, J.-A., Jeannin, M., Sabot, R., Rémazeilles, C., Refait, P. (2008) Characterisation of mackinawite by Raman spectroscopy: Effects of crystallisation, drying and oxidation. *Corrosion Science* 50, 3247–3255. https://doi.org/10.1016/j.corsci.2008.08.041

Bourdoiseau, J.-A., Jeannin, M., Rémazeilles, C., Sabot, R., Refait, P. (2011) The transformation of mackinawite into greigite studied by Raman spectroscopy. *Journal of Raman Spectroscopy* 42, 496–504. https://doi.org/10.1002/jrs.2729

Csákberényi-Malasics, D., Rodriguez-Blanco, J.D., Kis, V.K., Rečnik, A., Benning, L.G., Pósfai, M. (2012) Structural properties and transformations of precipitated FeS. *Chemical Geology* 294–295, 249–258. https://doi.org/10.1016/j.chemgeo.2011.12.009

Duverger, A., Berg, J.S., Busigny, V., Guyot, F., Bernard, S., Miot, J. (2020) Mechanisms of Pyrite Formation Promoted by Sulfate-Reducing Bacteria in Pure Culture. *Frontiers in Earth Science* 8, 588310. https://doi.org/10.3389/feart.2020.588310

Flynn, T.M., O'Loughlin, E.J., Mishra, B., DiChristina, T.J., Kemner, K.M. (2014) Sulfur-mediated electron shuttling during bacterial iron reduction. *Science* 344, 1039–1042. https://doi.org/10.1126/science.1252066

Galić, A., Mason, P.R.D., Mogollón, J.M., Wolthers, M., Vroon, P.Z., Whitehouse, M.J. (2017) Pyrite in a sulfate-poor Paleoarchean basin was derived predominantly from elemental sulfur: Evidence from 3.2 Ga sediments in the Barberton Greenstone Belt, Kaapvaal Craton. *Chemical Geology* 449, 135–146. https://doi.org/10.1016/j.chemgeo.2016.12.006

Kappler, A., Bryce, C., Mansor, M., Lueder, U., Byrne, J.M., Swanner, E.D. (2021) An evolving view on biogeochemical cycling of iron. *Nature Reviews Microbiology* 19, 360–374. https://doi.org/10.1038/s41579-020-00502-7

Kraal, P., van Genuchten, C.M., Behrends, T. (2022) Phosphate coprecipitation affects reactivity of iron (oxyhydr)oxides towards dissolved iron and sulfide. *Geochimica et Cosmochimica Acta* 321, 311–328. https://doi.org/10.1016/j.gca.2021.12.032

Lepot, K. (2020) Signatures of early microbial life from the Archean (4 to 2.5 Ga) eon. *Earth-Science Reviews* 209, 103296. https://doi.org/10.1016/j.earscirev.2020.103296

Liu, Y., Zhao, Q., Liao, C., Tian, L., Yan, X., Li, N., Wang, X. (2023) Anaerobic bioreduction of elemental sulfur improves bioavailability of Fe(III) oxides for bioremediation. *Science of the Total Environment* 858, 159794. https://doi.org/10.1016/j.scitotenv.2022.159794

Mansor, M., Berti, D., Hochella Jr., M.F., Murayama, M., Xu, J. (2019) Phase, morphology, elemental composition and formation mechanisms of biogenic and abiogenic Fe-Cu-sulfide nanoparticles: A comparative study on their occurrences under anoxic conditions. *American Mineralogist* 104, 703–717. https://doi.org/10.2138/am-2019-6848

Miller, N., Dougherty, M., Du, R., Sauers, T., Yan, C., *et al.* (2020) Adsorption of Tetrathiomolybdate to Iron Sulfides and Its Impact on Iron Sulfide Transformations. *ACS Earth and Space Chemistry* 4, 2246–2260. https://doi.org/10.1021/acsearthspacechem.0c00176

Nie, Z., Wang, N., Xia, X., Xia, J., Liu, H., Zhou, Y., Deng, Y., Xue, Z. (2020) Biogenic FeS promotes dechlorination and thus de-cytotoxity of trichloroethylene. *Bioprocess and Biosystems Engineering* 43, 1791–1800. https://doi.org/10.1007/s00449-020-02369-7

Peiffer, S., Behrends, T., Hellige, K., Larese-Casanova, P., Wan, M., Pollok, K. (2015) Pyrite formation and mineral transformation pathways upon sulfidation of ferric hydroxides depend on mineral type and sulfide concentration. *Chemical Geology* 400, 44–55. https://doi.org/10.1016/j.chemgeo.2015.01.023

Philippot, P., Van Zuilen, M., Lepot, K., Thomazo, C., Farquhar, J., Van Kranendonk, M.J. (2007) Early Archaean Microorganisms Preferred Elemental Sulfur, Not Sulfate. *Science* 317, 1534–1537. https://doi.org/10.1126/science.1145861

Picard, A., Gartman, A., Girguis, P.R. (2016) What Do We Really Know about the Role of Microorganisms in Iron Sulfide Mineral Formation? *Frontiers in Earth Science* 4, 68. https://doi.org/10.3389/feart.2016.00068

Son, S., Hyun, S.P., Charlet, L., Kwon, K.D. (2022) Thermodynamic stability reversal of iron sulfides at the nanoscale: Insights into the iron sulfide formation in low-temperature aqueous solution. *Geochimica et Cosmochimica Acta* 338, 220–228. https://doi.org/10.1016/j.gca.2022.10.021

Stöckl, M., Teubner, N.C., Holtmann, D., Mangold, K.-M., Sand, W. (2019) Extracellular Polymeric Substances from *Geobacter sulfurreducens* Biofilms in Microbial Fuel Cells. *ACS Applied Materials and Interfaces* 11, 8961–8968. https://doi.org/10.1021/acsami.8b14340

Subramani, T., Lilova, K., Abramchuk, M., Leinenweber, K.D., Navrotsky, A. (2020) Greigite (Fe_3S_4) is thermodynamically stable : Implications for its terrestrial and planetary occurrence. *Proceedings of the National Academy of Sciences* 117, 28645–28648. https://doi.org/10.1073/pnas.2017312117

Tomaszewski, E.J., Olson, L., Obst, M., Byrne, J.M., Kappler, A., Muehe, E.M. (2020) Complexation by cysteine and iron mineral adsorption limit cadmium mobility during metabolic activity of *Geobacter sulfurreducens*. *Environmental Science: Processes and Impacts* 22, 1877–1887. https://doi.org/10.1039/D0EM00244E

Troelsen, H., Jørgensen, B.B. (1982) Seasonal dynamics of elemental sulfur in two coastal sediments. *Estuarine, Coastal and Shelf Science* 15, 255–266. https://doi.org/10.1016/0272-7714(82)90062-2

van Gemerden, H., Tughan, C.S., de Wit, R., Herbert, R.A. (1989) Laminated microbial ecosystems on sheltered beaches in Scapa Flow, Orkney Islands. *FEMS Microbiology Ecology* 5, 87–101. https://doi.org/10.1111/j.1574-6968.1989.tb03661.x

Wang, X., Liu, F., Tan, W., Li, W., Feng, X., Sparks, D.L. (2013) Characteristics of Phosphate Adsorption-Desorption Onto Ferrihydrite: Comparison With

Well-Crystalline Fe (Hydr)Oxides. *Soil Science* 178, 1–11. https://doi.org/10.1097/SS.0b013e31828683f8

Wang, X.-N., Sun, G.-X., Li, X.-M., Clarke, T.A., Zhu, Y.-G. (2018) Electron shuttle-mediated microbial Fe(III) reduction under alkaline conditions. *Journal of Soils and Sediments* 18, 159–168. https://doi.org/10.1007/s11368-017-1736-y

Ye, L., Jing, C. (2022) Iron(III) reducing bacteria immobilise antimonite by respiring elemental sulfur. *Geochemical Perspectives Letters* 21, 37–41. https://doi.org/10.7185/geochemlet.2215

Geochemical Perspectives Letters

Co-reduction of Fe(III) and S^0 drives Fe-S biomineral formation and phosphate mobilisation

R. Bronner, K. Thompson, C. Dreher, E. Runge, E. Voggenreiter, J. Shuster, B. Wan, P. Joshi, S. Fischer, J.-P. Duda, A. Kappler, M. Mansor

Supplementary Information

The Supplementary Information includes:

- Materials and Methods
- Supplementary Discussion
- Tables S-1 and S-2
- Assignment of Mineral Phases *via* Mössbauer Spectroscopy
- Figures S-1 to S-5
- Supplementary Information References

Materials and Methods

Microbes and minerals. *Geobacter sulfurreducens* and ferrihydrite were prepared as previously described (Tomaszewski *et al.*, 2020). Briefly, *G. sulfurreducens* was pre-grown in a bicarbonate buffered medium with acetate (25 mM) supplied as an electron donor and fumarate (40 mM) as an electron acceptor for 5 days at 28 °C prior to transfer into the experimental setups. Ferrihydrite minerals were synthesised *via* titration of $FeCl_3$ with 1 M KOH to pH 7.5 and resuspended in anoxic MQ H_2O after several rounds of H_2O washes. Elemental sulfur (S^0; Sigma Aldrich product #13803) was sterilised by pasteurising for 30 minutes at 90 °C and then kept in the glovebox (MBraun; 100 % N_2) to fully allow adsorbed O_2 removal over time.

Experimental setup. The base medium used for the experiment contained KH_2PO_4 (4.4 mM), NH_4Cl (5.6 mM), $MgSO_4 \cdot 7\ H_2O$ (2 mM), $CaCl_2 \cdot 2\ H_2O$ (0.7 mM), Na-acetate (25 mM), $NaHCO_3$ (30 mM as buffer) and 1 mL/L each of trace elements SL10, 7 vitamin solution and selenite tungstate solution (Tomaszewski *et al.*, 2020). While bubbling with N_2/CO_2, the medium was aliquoted into three separate portions and the pH was adjusted to the target values (pH 6.5, 7.2 and 8.0) with the addition of 1 M HCl or 5 M KOH. The pH values were chosen to study the effect of different pH and microbial rates of S^0 and Fe(III) reduction on the formation of Fe sulfide minerals. While maintaining anoxic conditions with continuous N_2/CO_2 bubbling, 50 mL of the medium was dispensed into 100 mL serum bottles, which were sealed with butyl rubber stoppers and transferred into a glovebox. Once inside the glovebox, the bottles were uncapped and 10 mg of pasteurised S^0 was added to the bottles. The bottles were recapped with the stoppers and sealed

with aluminium crimps. Finally, ferrihydrite (~3 mL) and pre-grown *G. sulfurreducens* (~5 mL) were injected into the bottles. For each pH value, five biological replicates (three for geochemical sampling and two for mineralogical analyses) and one abiotic control (no cells added) were prepared. The bottles were incubated at 28 °C for the duration of the experiment (42 days). Each bottle contained 60 mM of S^0 and 30 mM of ferrihydrite as electron acceptors. The concentration of S^0 is higher than typically found in sediments (1–10 mM; Zopfi *et al.*, 2004; Ye and Jing, 2022) but comparable to in microbial mats (Troelsen and Jørgensen, 1982; van Gemerden *et al.*, 1989), while the concentration of ferrihydrite is comparable to HCl-extractable Fe in sediments (30–40 mM after converting from weight percentage and accounting for porosity; Raiswell and Canfield, 1998). Given the stoichiometry of acetotrophic S^0 and Fe(III) reduction (Reactions 1 and 2), the supplied 25 mM acetate should theoretically support full reduction of the S^0 and Fe(III) from ferrihydrite.

(1) Acetotrophic ferrihydrite reduction

$$CH_3COO^- + 8\ Fe(OH)_3 + 15\ H^+ \rightarrow 2\ HCO_3^- + 8\ Fe^{2+} + 20\ H_2O$$

(2) Acetotrophic S^0 reduction

$$CH_3COO^- + 4\ S^0 + 4\ H_2O \rightarrow 2\ HCO_3^- + 5\ H^+ + 4\ HS^-$$

Geochemical sampling. All samplings were conducted under anoxic condition in the glovebox. Aliquots (2 mL) from each bottle were sampled two to three times a week. Samples were centrifuged at 12,000 *g* for 5 minutes. The supernatants were sub-aliquoted for analysis of dissolved Fe^{2+} and phosphate (dilution in 1 M HCl) and dissolved sulfide (fixed with 20 % zinc acetate). The solid pellets were dissolved in 6 M HCl overnight in a closed vial. Samples were stored at 4 °C until analysis. Additionally, pH values of unpreserved samples were determined with a pH meter at certain timepoints.

Dissolved Fe^{2+} and total Fe concentrations were measured using a ferrozine method (Hegler *et al.*, 2008). Notably, dissolved Fe^{2+} samples (including abiotic controls) showed elevated values (1.5 mM) at day 0 and were therefore not considered in the interpretation. Subsequent Fe^{2+} concentrations from abiotic controls were on average 55 ± 55 µM (n = 36 across all three pH values and timepoints), indicating low concentrations throughout. Additionally, measurements of HCl-extractable Fe can yield elevated Fe(II) contents because solid-phase sulfide can reduce Fe^{3+} during HCl extraction (Peiffer *et al.*, 2015; Kraal *et al.*, 2022). Nevertheless, an increase in HCl-extractable Fe(II)/Fe(total) ratio can still reflect increasingly reducing conditions in our cultures.

Dissolved total sulfide ($H_2S + HS^- + S^{2-}$) was measured using a modified methylene blue method (Cline, 1969). To samples fixed with Zn-acetate (1 mL), 200 µL ADMA, 200 µL Fe(III) solution and 580 µL H_2O were added in sequence. The samples were incubated for 30 minutes in the dark before measuring the absorbance at 665 nm. Standards used for calibration were prepared by dissolving $Na_2S \cdot 9\ H_2O$ salt in anoxic H_2O and fixed by the addition of Zn-acetate. The stock solution standard concentration was verified by iodometric titration (USGS, 1985). Dissolved phosphate was measured *via* a modified phosphomolybdate colourimetric assay (Murphy and Riley, 1962). Each sample was measured in triplicates in 96-well plates. Samples (20 µL) were mixed with ascorbic acid (40 µL) and acidic molybdate solution (140 µL), incubated in the dark for 20 minutes, and then measured for absorbances at 700 nm.

Mineralogical analyses. The presence of magnetic minerals was assessed by holding a hand magnet to the side of the bottles (Fig. S-1). The magnetism strength was assigned as "weak" or "strong" subjectively based on the amount and the speed of the minerals' attraction to the applied magnet.

The bottles were sampled for mineralogy after 21 and 42 days of incubation. For micro-XRD (Bruker's D8 Discover GADDS XRD2; cobalt Kα radiation source), about 2–5 mL of sample was taken separately from each bottle. The solids were pelleted by centrifugation, washed three times with H_2O to remove traces of salt and allowed to dry in a glovebox. Individual scans of the dry sample were collected from 5–60° 2θ with a collection time of 240 seconds. All scans were collected within 8 hours of removal from the anoxic glovebox, which was well below the time reported for

conversion of dry mackinawite *via* oxidation to other phases (Boursiquot *et al.*, 2001). Mineral identification was based on the database in Match! (version 3.13) except for nano-mackinawite, which was based on Lennie *et al*. (1995).

For scanning electron microscopy (SEM) and energy dispersive X-ray spectroscopy (EDS) analysis, samples were prepared *via* two methods. The first method was designed to minimise oxidation, in which centrifugation and water washes were performed as described above under anoxic conditions. The samples were immediately coated with ~8 nm of platinum using a BAL-TEC^{TM} SCD 005 sputter coater upon removal from the glovebox to minimise O_2 exposure and to reduce charging effects during analysis. The second method was designed to better preserve cellular structure. Samples were fixed in 2.5 $\%_{(aq)}$ electron microscopy-grade glutaraldehyde at 4 °C for 24 hours. Poly-lysine coated glass slides were prepared in advance by placing 30 µL of 1 % poly-lysine solution onto clean glass slides that were glow discharged using a Pelco easiGlow^{TM} glow discharge system. The glass slides were dried in a drying oven at 50 °C for 1 hr and placed into a 96-well plate with the coated side facing up. An aliquot (30 µL) of sample was placed onto separate poly-lysine coated glass slides and incubated for 15 min to allow minerals and cells to settle and attach to the poly-lysine coating. The samples were dehydrated using ethanol. Briefly, 500 µL of 25 % ethanol was added to a well containing sample on a glass slide and allowed to incubate for 15 min. After incubation the solution was removed and replaced with 50 % ethanol and re-incubated. This sequential procedure was repeated using 75 % and 3× 100 % ethanol. After the final ethanol dehydration, a mixture of 100 % ethanol (250 µL) and hexamethyldisiloxane (HMDS, 250 µL) was added to each well and the sample were incubated for 30 min. After incubation, this solution was discarded and replaced with 100 % HMDS (250 µL) and allowed to air dry overnight by leaving the 96-well plate partially uncovered. Once dry, the glass slides were attached to aluminium stubs using carbon adhesive tabs and the samples were coated with platinum. Mineral structure and associated microbes were characterised using a Zeiss Crossbeam 550L Scanning Electron Microscope (SEM) equipped with Oxford Instrument Energy Dispersive Spectrometer (EDS). Micrographs were taken in Secondary Electron (SE) mode with accelerating voltage of 2 kV. Elemental composition of minerals was obtained by EDS (point scans) and using an accelerating voltage of 15 or 20 kV. The mineralogy of precipitates observed *via* SEM and stated in Figure 2 was assigned based on the combined evidence of XRD, Mössbauer, EDS and morphology. The second method showed evidence for partial oxidation (*i.e.* orange colour of precipitates at the periphery). Overall, however, no clear differences in mineral morphology were observed between the first and the second methods and between Day 21 and 42 samples.

For Mössbauer spectroscopy, ~10 mL of mineral suspension was separately collected onto 0.22 µm pore size mixed cellulose ester filters. Solids collected on the filters were wrapped with Kapton tapes (O_2-impermeable) and stored at −20 °C before insertion into a closed-cycle exchange gas cryostat (Janis cryogenics) under a backflow of He to minimise exposure to air. Spectra were collected at 77 K and 6 K using a constant acceleration drive system (WissEL) in transmission mode with a ^{57}Co/Rh source. All spectra were calibrated against a 7 µm-thick ^{57}Fe foil that was measured at room temperature. Analysis was carried out using Recoil (University of Ottawa) and the extended Voigt Based Fitting (VBF) routine (Lagarec and Rancourt, 1997). The half width at half maximum (HWHM) was constrained to 0.138 mm/s during fitting.

To investigate the mineralogy of the black residue remaining after 6 M HCl extraction, the residue was resuspended in 25 µL H_2O and dried onto a glass slide. Raman spectroscopy (WITec GmbH®, Ulm, Germany) was collected at 532 nm wavelength using a low laser power of 1 mW, 10 accumulations and 20 seconds integration time to avoid thermal alteration.

Supplementary Discussion

Interrelated pH-dependent processes affecting biogeochemical evolution. Here, we attempt to consider all the different factors that can affect the geochemical trends (timing of the ferruginous-sulfide transition and the maximum Fe^{2+} and sulfide produced) observed in bottles starting at different pH values. We first consider factors affecting microbial activities. The optimal growth pH for *G. sulfurreducens* and other *Geobacter* species are reportedly around pH 7 (Straub *et al.*, 1998; Sung *et al.*, 2006; Kim and Lee, 2010). Additionally, direct microbial Fe(III) reduction is thermodynamically more favourable than S^0 at pH < 8, although the specific pH threshold depends on the availability of the electron donor (Flynn *et al.*, 2014). Therefore, these two factors will lead to the expectation of lower Fe^{2+} and higher sulfide at pH 8.0 compared to at pH 6.5 and 7.2 (note that the final pH of these two bottles were 7.1 and 7.5, respectively, meaning they are quite similar), consistent with the observations (Fig. 1**)**. SEM observations support this conclusion, with more cells attached to S^0 globules with increasing pH (Fig. S-3). Cells did not exhibit extracellular mineralisation but were closely associated with nanophase Fe minerals as identified *via* energy dispersive X-ray spectroscopy (EDS). We were not able to clearly identify whether the cells prefer to reduce S^0 or Fe(III) at different pH values, given the similar net effect of Fe(II) production due to direct (microbial) and indirect (sulfide-mediated) Fe(III) reduction. It is likely that different populations of cells within the same bottle could utilise different electron acceptors due to local variability in mineral access or overlapping thermodynamic potentials, especially when electron donors were available in excess.

It must be kept in mind that a series of abiotic processes are occurring simultaneously. First, the released Fe^{2+} can be adsorbed onto ferrihydrite, with more adsorption expected with increasing pH (ferrihydrite has a point of zero charge of ~8.0; Hiemstra, 2013). At the same time, Fe^{2+} adsorption onto Fe(III) minerals is known to trigger Fe^{2+}-catalysed recrystallisation, with more pronounced effects with increasing pH (Handler *et al.*, 2014). This process can result in the formation of more thermodynamically stable phases such as lepidocrocite, magnetite and goethite (Peiffer *et al.*, 2015). Their formation would have led to decreased surface areas for Fe^{2+} adsorption and the reactivity of Fe(III) minerals with respect to both direct (microbial) and indirect (sulfide-mediated) reduction. No such phases were found in our experiments, but we cannot rule out their formation in the early stages before day 21.

Second, the sulfide produced from microbial S^0 reduction can react with Fe(III) minerals to produce Fe(II) in a process termed indirect sulfide-mediated Fe(III) reduction (Reaction 3).

(3) Indirect sulfide-mediated Fe(III) reduction

$$2\ Fe(OH)_3 + HS^- + 5\ H^+ \rightarrow 2\ Fe^{2+} + S^0 + 6\ H_2O$$

The rate of this reaction is controlled by the dominant surface species of ferrihydrite (*e.g.*, [>FeOH] vs [$>FeOH_2^+$]) and the aqueous speciation of sulfide (H_2S *vs*. HS^-), with a pH optimum around 6.5 (Poulton, 2003). Therefore, more Fe^{2+} and lower sulfide are expected at pH 6.5 and 7.2 compared to pH 8.0. However, this reaction can also generate a surface coating of FeS that may inhibit both direct and indirect Fe(III) reduction, thus affecting the accumulation rate of Fe^{2+} and sulfide in solution. Other studies have also shown that Fe(III) minerals with FeS surface coatings are still accessible to reduction given that microbes can utilise FeS as an electron conduit (Deng *et al.*, 2020; Zhu *et al.*, 2022).

Finally, the observed geochemical trends also depend on the rate of mineral formation and dissolution. Mackinawite precipitation rate is expected to be pH-independent above pH 7 and slower at lower pH (Reaction 4; Rickard and Luther, 2007). The transformation of mackinawite to greigite likely proceeds *via* solid-state transformation, with faster rates at lower pH (Reaction 4; Rickard and Luther, 2007; Bourdoiseau *et al.*, 2011). The precipitation rate of vivianite is expected to be faster with increasing pH based on solubility considerations (Reaction 6; Goedhart *et al.*, 2022). Finally, the rate of sulfide-mediated vivianite dissolution is likely to be pH-independent at near-neutral pH and mainly controlled by sulfide availability (Reaction 7).

(4) FeS precipitation

$Fe^{2+} + HS^- \rightarrow FeS + H^+$

(5) FeS transformation to greigite

$3\ FeS + S^0 \rightarrow Fe_3S_4$

(6) Vivianite precipitation

$3\ Fe^{2+} + 2\ HPO_4^{2-} \rightarrow Fe_3(PO_4)_2 + 2\ H^+$

(7) Sulfide-mediated vivianite dissolution

$Fe_3(PO_4)_2 + 2\ HS^- \rightarrow 2\ FeS + 2\ HPO_4^{2-} + Fe^{2+}$

We summarise the expected effects of all these biotic and abiotic processes to net Fe^{2+} accumulation in Table S-1. This exercise illustrates that we will predict the highest maximum Fe^{2+} at pH 6.5 > pH 7.2 > pH 8.0. Intuitively, we will also predict longer ferruginous-sulfide transition timing and lower maximum dissolved sulfide in the same pH order. While this exercise correctly predicts the trend observed at pH 8.0, it fails to explain why the pH 7.2 cultures exhibited higher maximum Fe^{2+} and longer transition time compared to the pH 6.5 cultures. The interconnectedness of all these reactions necessitates a more complex biogeochemical model to elucidate the specific mechanisms. Nonetheless, the net impact on biomineral formation and phosphate release are readily observable *via* the techniques employed in this study.

Decrease in magnetism over time. In all cultures, the magnetism decreased noticeably after 27 days. One explanation is the early formation of magnetite (Fe_3O_4) as commonly observed during ferrihydrite reduction by *Geobacter* species (Byrne *et al.*, 2015). Magnetite has a higher intrinsic magnetism than greigite (Roberts *et al.*, 2011), such that the decrease in magnetism could reflect transformation of magnetite to greigite. However, XRD and Mössbauer showed no evidence for magnetite, which should have been present at day 21. The second possibility is due to the transformation of greigite to mackinawite over time, given that mackinawite is more thermodynamically stable under highly reducing conditions (Rickard and Luther, 2007). Additionally, particle properties (*e.g.*, size and crystallinity) can change over time, thereby influencing greigite's magnetic properties (Roberts *et al.*, 2011). The fate of greigite will be important to study in the future for its potential preservation or transformation to other stable phases such as pyrite.

The absence of biogenic pyrite. In our experiments, pyrite was not detectable by XRD and Mössbauer. Given the detection limit of both techniques (~5 wt. %), we probed for the presence of trace pyrite based on its poor solubility in HCl. Our data showed decreasing HCl extraction efficiency over time, with <20 % of Fe extractable after 20 days relative to initial time points (Fig. S-2e). Small amounts of black residue remained after HCl extraction and was identified as pure S^0 *via* Raman spectroscopy (Fig. S-4). Black S^0 can form as a product of abiotic oxidation of mackinawite (or the released sulfide) in HCl, and this seems to be associated with poor Fe recovery (Rickard et al., 2006). Overall, we could not detect pyrite in our experiments.

Besides the reasons discussed in the main text, other factors should be considered for the absence of pyrite. The first is the kinetics of pyrite precipitation, for which there remains a huge uncertainty. Compilation of estimates from radio-labelled sulfur isotopes suggests average precipitation rates on the order of months in sediments (Mansor and Fantle, 2019), while a diffusion-nucleation model suggests that it takes only 3–5 days for an average framboid to form (Rickard, 2019). Predicted precipitation rates based on rate constants determined from lab experiments are too slow (*i.e.* years; Rickard and Luther, 2007; Wan *et al.*, 2017; Mansor and Fantle, 2019). In recent years, several studies have observed the precipitation of biogenic pyrite within weeks to months in lab cultures (Thiel *et al.*, 2019; Berg *et al.*, 2020; Duverger *et al.*, 2020; Allen *et al.*, 2021), which are slightly faster compared to the aforementioned average rates in sediments. The activity of microorganisms are known to promote pyrite precipitation, even within two weeks (Canfield

et al., 1998), and the conditions in that study (30 mM ferrihydrite and 150 mM S^0 incubated with a sulfur-disproportionater) are most similar to ours. Our study employed 42 days (6 weeks) of incubation period, which we hypothesised to be close to the earliest time required for pyrite precipitation. Continuous observation of the cultures, which are now over 1 year old, showed no changes from small blackish minerals (indicative of mackinawite/greigite) to greyish minerals with larger particle sizes (indicative of pyrite).

Pyrite formation could also be inhibited by the presence of certain organics, specifically aldehydes (Rickard *et al.*, 2001; Wang *et al.*, 2015) and phosphate-containing organics (Harmandas *et al.*, 1998). Different EPS compositions and metabolites produced by microorganisms may therefore strongly influence pyrite precipitation rates.

Supplementary Tables

Table S-1 Summary of the various factors that affect the biogeochemical evolution observed in the cultures. Arrows denote the relative effect on Fe^{2+} accumulation in solution among the three conditions considered (initial pH 6.5, 7.2 and 8.0), with '↑' indicating increased, '↓' indicating lowered and '↔' indicating in-between. All the effects are summarised to make predictions that are compared to experimental data.

Process	Initial pH		
	6.5	7.2	8.0
Optimal growth pH	↑	↑	↓
Direct Fe(III) reduction	↑	↑	↓
Fe^{2+} adsorption	↑	↔	↓
Fe^{2+}-catalysed recrystallisation to minerals with lower surface areas	↓	↔	↑
Indirect (sulfide-mediated) reduction	↑	↔	↓
FeS precipitation	↑	↓	↓
Vivianite precipitation	↓	↔	↑
Summary of net effect	4↑ 2↓	2↑ 3↔ 1↓	2↑ 4↓
Prediction for maximum Fe^{2+}	Highest	Middle	Lowest
Experimental data for maximum Fe^{2+}	Middle	Highest	Lowest

Table S-2 Results of Mössbauer fitting. CS, centre shift; QS, quadrupole splitting; H (T), hyperfine field; χ^2, goodness of fit.

Sample	*T* (K)	Site	CS (mm/s)	QS (mm/s)	H (T)	Relative area (%)	χ^2
pH 8 D21	77	FeS	0.45	0.41		16.54	1.16
		Fe(II)	1.15	2.82		12.89	
		greigite tetra	0.37	0.01	28.63	13.28	
		greigite octa	0.71	-0.03	32.69	3.711	
		FeS_x	0.48	-0.09	27.40	53.59	
	6	Fe(II)	1.25	2.81		7.55	1.54
		greigite tetra	0.35	0.00	28.73	15.08	
		greigite octa	0.69	-0.06	29.46	6.287	
		FeS_x	0.48	0.00	22.63	71.08	
pH 8 D42	77	vivianite I	1.28	2.80		5.09	1.72
		vivianite II	1.35	3.40		2.24	
		greigite tetra	0.37	0.00	29.14	23.14	
		greigite octa	0.71	-0.06	33.10	8.53	
		FeS_x	0.48	-0.02	21.06	60.99	
	6	Fe(II)	1.20	2.80		0.00	3.39
		greigite (tetra)	0.40	0.00	31.14	29.50	
		greigite (octa)	0.72	-0.06	33.36	13.80	
		vivianite	1.10	2.42	7.98	8.20	
		FeS_{x2}	0.48	-0.02	25.54	17.30	
		FeS_{x1}	0.46	-0.03	17.40	31.20	
pH 7 D42	77	FeS	0.51	0.29		9.34	0.85
		vivianite I	1.35	2.82		15.7	
		vivianite II	1.42	3.45		12.6	
		gregeit (tetra)	0.41	-0.01	30.14	32.64	
		gregeit (octa)	0.71	-0.02	33.63	20.1	
		FeS_x	0.41	0.03	13.27	9.58	
	6	not feasible to fit					n.d.
pH 6 D42	77	FeS	0.44	0.24		10.03	1.7
		vivianite I	1.35	2.87		9.99	
		greigite (tetra)	0.37	0.00	29.40	17.3	
		greigite (octa)	0.71	-0.02	33.13	12.5	
		FeS_x	0.36	0.03	22.12	50.1	
	6	FeS	0.47	0.13		3.32	3.16
		greigite (tetra)	0.37	0.00	30.03	24.64	
		greigite (octa)	0.72	-0.02	33.15	5.42	
		vivianite	1.36	2.40	10.73	8.67	
		FeS_{x1}	0.46	-0.06	24.96	47.28	
		FeS_{x2}	0.62	-0.24	27.33	10.65	

Assignment of Mineral Phases *via* Mössbauer Spectroscopy

The Mössbauer spectra of the samples indicated the presence of iron sulfide phases and ferrous iron, evidenced by a mix of singlets, doublets, and sextets. The iron sulfide phases that were identified include greigite (Fe_3S_4), stoichiometric mackinawite (FeS), and nonstoichiometric mackinawite (often denoted as FeS_x). Ferrous iron was observed either in the form of Fe(II) or vivianite ($Fe_3(PO_4)_2$).

We first discuss the results of spectra collected at 77 K. We observed a doublet with a centre shift (CS) value of 1.2–1.3 mm/s and a quadrupole split (QS) of 2.7–2.9 mm/s, indicative of Fe(II) (Murad and Cashion, 2004). Since there were no clay minerals in the experimental setup, we exclude clay Fe(II) and assign this phase to adsorbed Fe(II). Adsorbed Fe(II) was present in the sample at pH 8 collected after day 21 (12.9 %) but not in other samples. We were able to differentiate between ferrous iron that was present in the form of vivianite as vivianite often exhibits parameters different than adsorbed Fe(II) or clay Fe(II) at 77 K (Mattievich and Danon, 1977). We fitted vivianite using one or two doublets according to Wilfert *et al*. (2016), with CS values ranging from 1.1 to 1.42 mm/s and the first doublet having a smaller QS value around 2.8, and the second doublet having a larger QS value around 3.4. Supporting evidence for the presence of vivianite was given by the spectra collected at 6 K (discussed further below) and XRD spectra and SEM graphs. Vivianite was not included as a fitting phase for sample pH 8 D21, since there was no evidence of a vivianite sextet in the 6 K spectra of the same sample, and fitting parameters characteristic of Fe(II) were better suited to fit this spectra. In all samples collected after D42, vivianite was present, with abundances ranging from 7.3 % to 28.3 %.

In samples collected at day 21 (pH 8) and day 42 (pH 6 and 7), we observed a singlet with CS values of 0.44–0.53 mm/s and QS values of 0.18–0.34 mm/s, characteristic of stoichiometric mackinawite FeS (Thiel *et al.*, 2019). Samples taken after day 42 (D42) showed decreasing FeS content with increasing pH: FeS had a relative abundance of 10.3 % at pH 6 but was not detectable anymore at pH 8.

In all samples, several sextets were also observed at 77 K, indicative of greigite and FeS_x (iron sulfides, sometimes denoted as nonstoichiometric mackinawite) phases. Greigite is typically best fitted with two separate sextets, indicative of the tetrahedral and octahedral Fe sites. Tetrahedral Fe in greigite had CS values of 0.35–0.41 mm/s, QS values of +0.01 to −0.01, and hyperfine field (H) values of 28.63–31.1 T while octahedral Fe had CS values of 0.69–0.72 mm/s, QS values of −0.02 to −0.06, and H values of 29.4–33.6 T (Vandenberghe *et al.*, 1992; Wan *et al.*, 2017). Greigite abundances ranged from 17.0 % to 52.7 %. FeS_x phases had less constrained parameters, and were detected in the form of a collapsed sextet. CS values ranged from 0.36 to 0.62 mm/s, QS values from −0.09 to +0.03, and H values from 13.3 to 27.4 T (Thiel *et al.*, 2019; Schröder *et al.*, 2020). FeS_x abundances ranged from 9.6 % to 61.0 %.

Spectra at 6 K allow us to partially identify phases that do not magnetically order at 77 K. Overall, 6 K spectra showed the presence of doublet and sextet features also detected at 77 K. Here, we note that several of the phases identified above have been shown to (partially) split from doublets to sextets, resulting in several overlapping sextets that cannot always be fit satisfactorily. Relative abundances of Fe(II) doublets and FeS singlets decreased from 77 K to 6 K, indicating that some of both these phases ordered at the lower temperature. This caused the detection of generally two sextets, likely corresponding to vivianite and another collapsed sextet. Vivianite at 6 K had CS values of 1.10–1.36 mm/s, QS values of 2.40–2.42, and H values from 8.0–10.7 T (Wilfert *et al.*, 2016). To achieve a satisfactory fit, another collapsed sextet was added at 6 K in all samples at 6 weeks after the start of the incubation, with CS values of 0.46–0.62 mm/s, QS values of −0.24 to −0.02 mm/s, and H values of 25.5–27.3 T. This sextet could possibly be another FeS_x phase (Thiel *et al*., 2019), or Fe(II) that was adsorbed on other mineral surfaces (Notini *et al.*, 2019). Vivianite had relative abundances of about 8 %, and the collapsed sextet was abundant from 10.6–31 %. The spectrum of pH 7 D42 at 6 K was not feasible to fit, since all trials with the existing Fe phases found in the other samples led to a poor fit, indicating quite a high uncertainty in phase assignments.

Differences between Fe phases at pH 8 between D21 and D42 indicate possible Fe sulfide mineral developments over time. Relative abundances of FeS and Fe(II) decrease over time from 16.5 % and 12.9 % to no detectable FeS and adsorbed/clay Fe(II). 7.3 % of Fe(II) at D42 was present in the form of vivianite (based on spectra collected at 77 K). Another collapsed FeS_x phase was needed to properly fit the 6 K spectra in the sample taken after D42 (but not after

D21). This may suggest that FeS_x phases become more heterogeneous over time, resulting in different Fe:S stochiometries involved which would lead to varying magnetic properties. Additionally, EPS (extracellular polymeric substances) or other microbial-derived organic matter could coat the surfaces of FeS_x phases, influencing their magnetic ordering at 6 K (Cornell and Schwertmann, 2003).

Collectively, the spectra at 6 K and 77 K suggest that the predominant Fe phases are Fe(II), vivianite, FeS, greigite and likely poorly crystalline FeS_x, with some differences at different pHs. The parameters of the phases and the relative areas are given in the Table S-2, along with the χ^2 value. This parameter describes the goodness of the fit, with an ideal value of 1. However, an ideal fit does not necessarily represent mineralogically realistic results, meaning values slightly above or below 1 might still represent the true Fe phases better. The χ^2 value for the fits were satisfactory for most samples (0.8–1.8), but poor (>3) for two samples at 6 K (pH 8 D42, pH 6 D42) due to the high number of different Fe phases. In such a system, we recommend quantitative interpretation of the 77 K spectra. For simplicity, we also visualise FeS and FeS_x as one component in Figure 3b.

Supplementary Figures

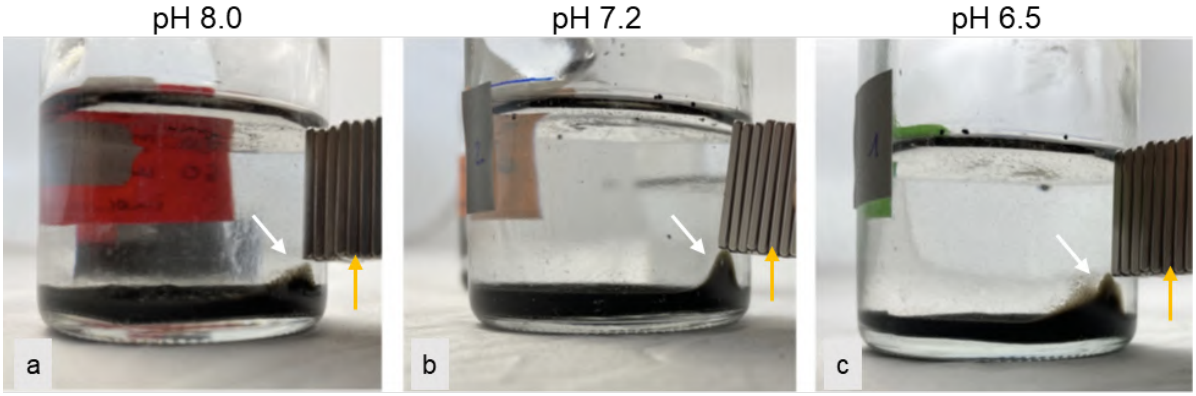

Figure S-1 Cultures after 14 days of incubation. Note the black colour of the solid materials. Magnetic minerals (denoted by white arrows) are observed between day 11 and 27 of incubation by holding magnet bars (yellow arrows) close to the bottles at all pH values. The particles aggregate over time and precipitates are observed on the glass wall at the headspace-solution interface.

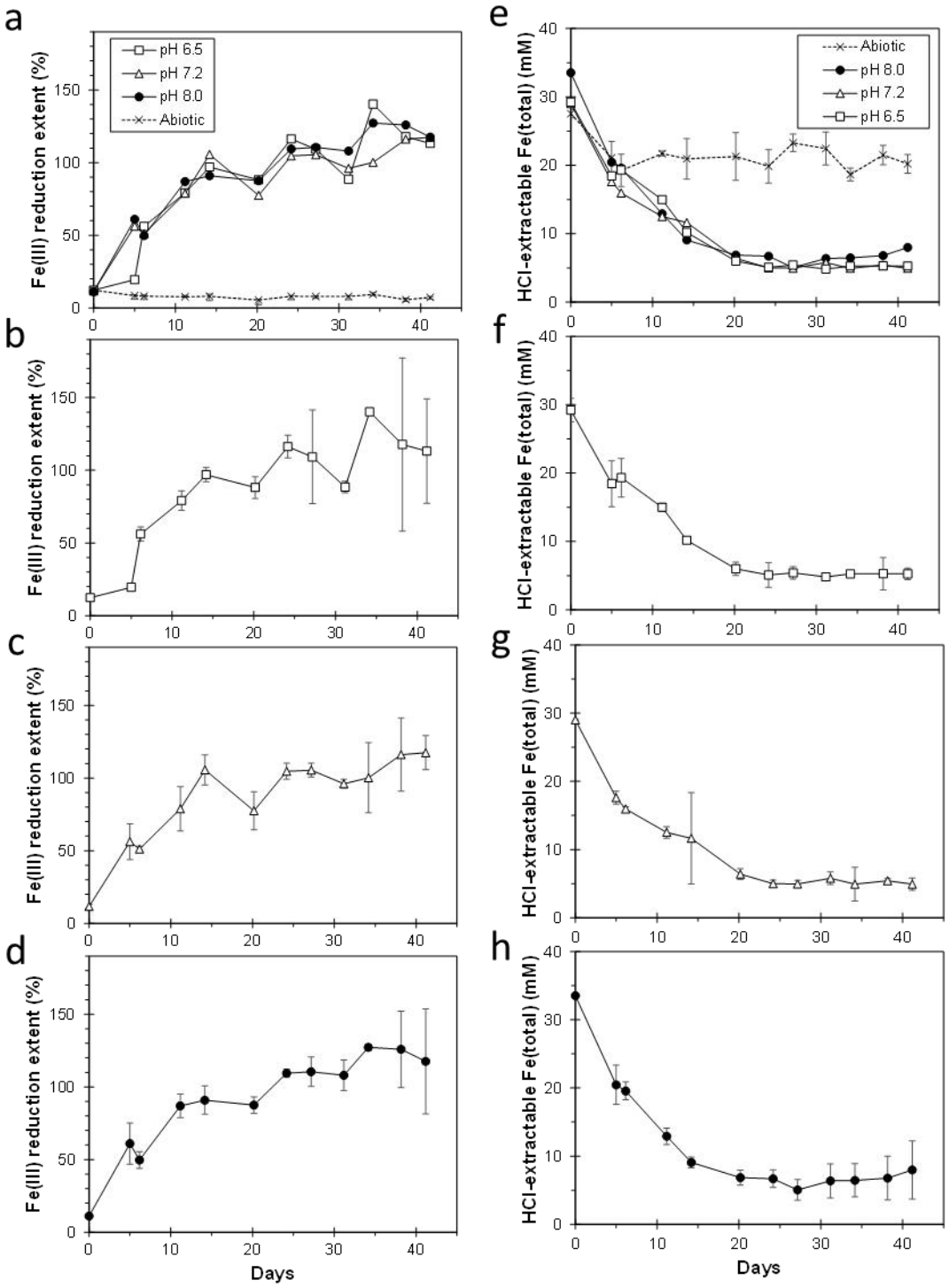

Figure S-2 Results from 6 M HCl-extractable Fe from the solid phase. **(a)** The Fe(III) reduction extent (from Fe(II)/Fe(total) ratio) indicated near-complete Fe(III) reduction within 15 days of incubation. **(b–d)** The same data at each pH value plotted individually with error bars. **(e)** The extractable Fe content showed a decrease over time in the culture bottles at all pH values, in contrast to the constant Fe content measured in the abiotic controls. **(f–h)** The same data at each pH values plotted individually with error bars. Abiotic controls were geochemically similar across pH values and were therefore averaged (n = 3) for the plots.

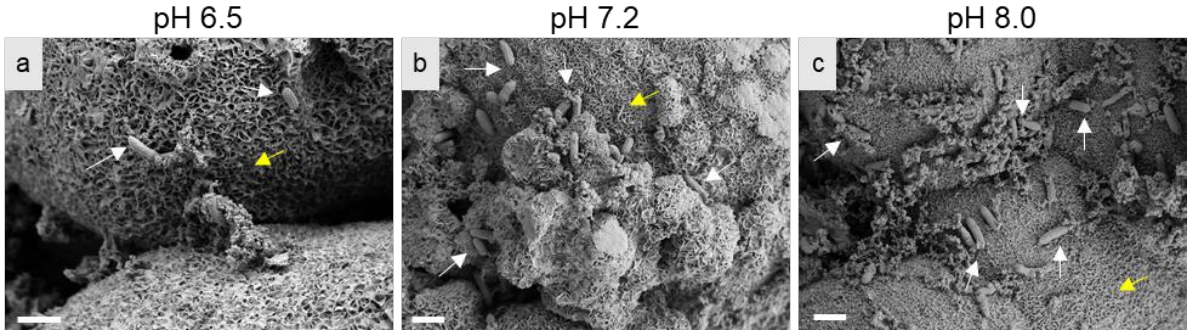

Figure S-3 SEM micrographs demonstrating *G. sulfurreducens* (white arrows) that appear attached to tens of micrometres-sized globules of S^0. The surface of these globules contained a multilayer coating of mackinawite (pseudo-honeycomb textures; yellow arrows). The number of cells associated with S^0 globules appear to increase with increasing pH, *i.e.* at **(a)** pH 6.5 compared to **(b)** pH 7.2 and **(c)** pH 8.0. Scale bar is 1 μm.

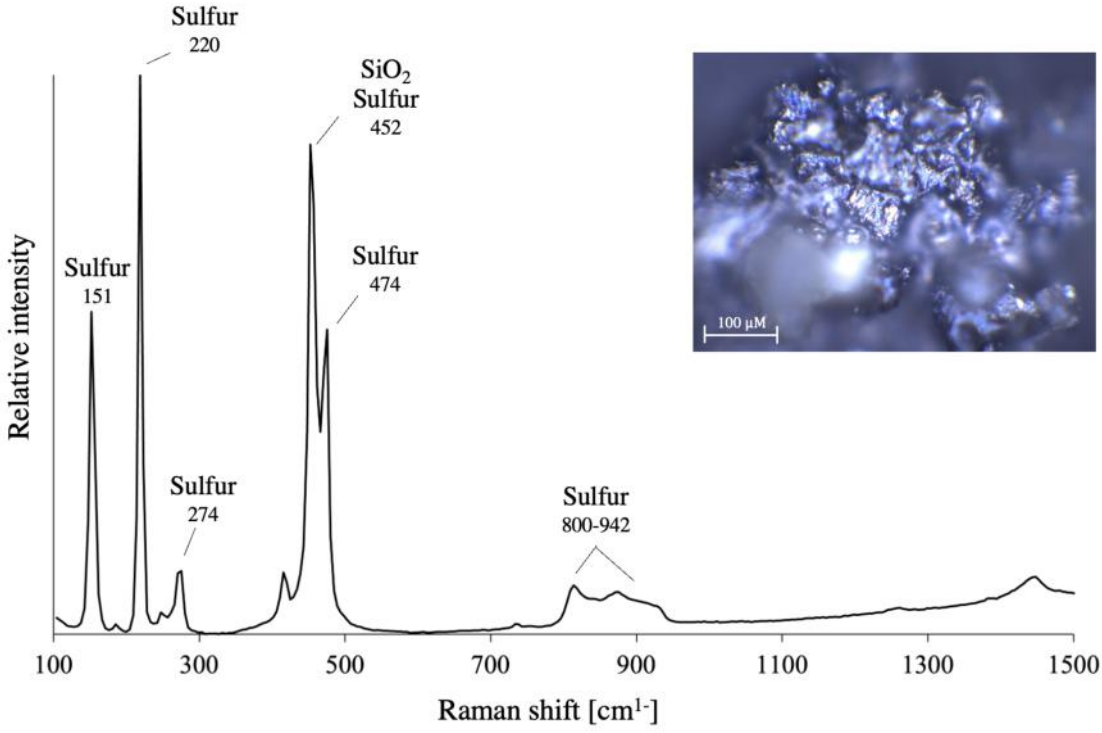

Figure S-4 Raman spectrum of the black residue from 6 M HCl extraction. The particles were identified as S^0 using the software CrystalSleuth, RRUFF database (https://rruff.info/; accessed 5 July 2022) and S^0 reference patterns provided in Nims *et al.* (2019). The signal at 452 cm^{-1} originates from SiO_2 from the glass slide, which overlaps with the S^0 signal. The picture at the top right shows a reflected light microscopy image of the black S^0 particles.

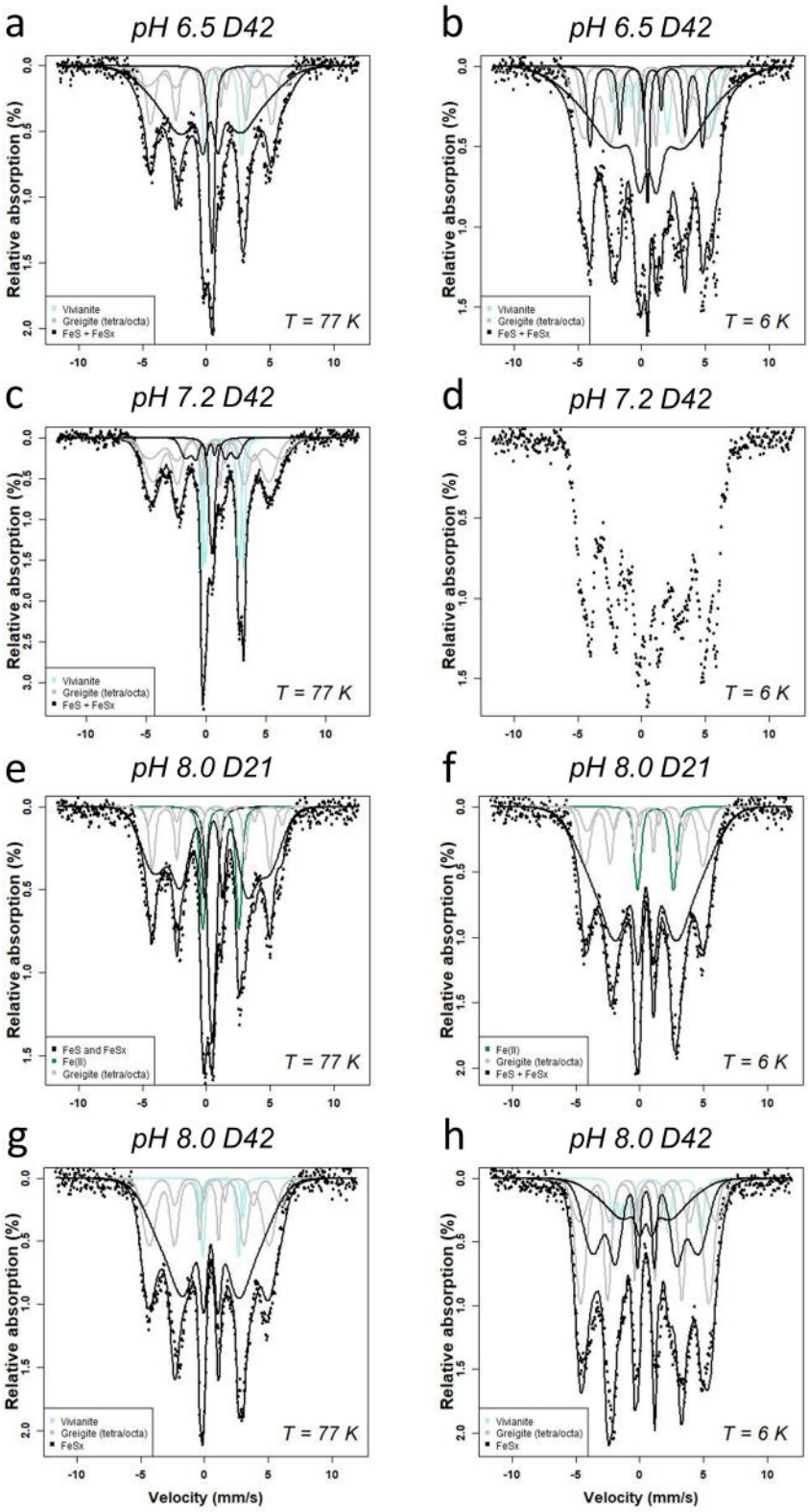

Figure S-5 Mössbauer spectra of all samples at 77 K (left side) and 6 K (right side). Markers indicate datapoints while different coloured lines indicate fitting results corresponding to each phase.

Supplementary Information References

Allen, K.D., Wegener, G., Sublett Jr., D.M., Bodnar, R.J., Feng, X., Wendt, J., White, R.H. (2021) Biogenic formation of amorphous carbon by anaerobic methanotrophs and select methanogens. *Science Advances* 7, eabg9739. https://doi.org/10.1126/sciadv.abg9739

Berg, J.S., Duverger, A., Cordier, L., Laberty-Robert, C., Guyot, F., Miot, J. (2020) Rapid pyritization in the presence of a sulfur/sulfate-reducing bacterial consortium. *Scientific Reports* 10, 8264. https://doi.org/10.1038/s41598-020-64990-6

Bourdoiseau, J.-A., Jeannin, M., Rémazeilles, C., Sabot, R., Refait, P. (2011) The transformation of mackinawite into greigite studied by Raman spectroscopy. *Journal of Raman Spectroscopy* 42, 496–504. https://doi.org/10.1002/jrs.2729

Boursiquot, S., Mullet, M., Abdelmoula, M., Génin, J.-M., Ehrhardt, J.-J. (2001) The dry oxidation of tetragonal FeS_{1-x} mackinawite. *Physics and Chemistry of Minerals* 28, 600–611. https://doi.org/10.1007/s002690100193

Byrne, J.M., Muhamadali, H., Coker, V.S., Cooper, J., Lloyd, J.R. (2015) Scale-up of the production of highly reactive biogenic magnetite nanoparticles using *Geobacter sulfurreducens*. *Journal of the Royal Society: Interface* 12, 20150240. https://doi.org/10.1098/rsif.2015.0240

Canfield, D.E., Thamdrup, B., Fleischer, S. (1998) Isotope fractionation and sulfur metabolism by pure and enrichment cultures of elemental sulfur-disproportionating bacteria. *Limnology and Oceanography* 43, 253–264. https://doi.org/10.4319/lo.1998.43.2.0253

Cline, J.D. (1969) Spectrophotometric determination of hydrogen sulfide in natural waters. *Limnology and Oceanography* 14, 454–458. https://doi.org/10.4319/lo.1969.14.3.0454

Cornell, R.M., Schwertmann, U. (2003) *The Iron Oxides: Structure, Properties, Reactions, Occurences and Uses*. Second Edition, WILEY-VCH Verlag GmbH & Co. KGaA, Weinheim. https://doi.org/10.1002/3527602097

Deng, X., Dohmae, N., Kaksonen, A.H., Okamoto, A. (2020) Biogenic Iron Sulfide Nanoparticles to Enable Extracellular Electron Uptake in Sulfate-Reducing Bacteria. *Angewandte Chemie* 132, 6051–6055. https://doi.org/10.1002/ange.201915196

Duverger, A., Berg, J.S., Busigny, V., Guyot, F., Bernard, S., Miot, J. (2020) Mechanisms of Pyrite Formation Promoted by Sulfate-Reducing Bacteria in Pure Culture. *Frontiers in Earth Science* 8, 588310. https://doi.org/10.3389/feart.2020.588310

Flynn, T.M., O'Loughlin, E.J., Mishra, B., DiChristina, T.J., Kemner, K.M. (2014) Sulfur-mediated electron shuttling during bacterial iron reduction. *Science* 344, 1039–1042. https://doi.org/10.1126/science.1252066

Goedhart, R., Müller, S., van Loosdrecht, M.C.M., van Halem, D. (2022) Vivianite precipitation for iron recovery from anaerobic groundwater. *Water Research* 217, 118345. https://doi.org/10.1016/j.watres.2022.118345

Handler, R.M., Frierdich, A.J., Johnson, C.M., Rosso, K.M., Beard, B.L., *et al*. (2014) Fe(II)-Catalyzed Recrystallization of Goethite Revisited. *Environmental Science and Technology* 48, 11302–11311. https://doi.org/10.1021/es503084u

Harmandas, N.G., Navarro Fernandez, E., Koutsoukos, P.G. (1998) Crystal Growth of Pyrite in Aqueous Solutions. Inhibition by Organophosphorus Compounds. *Langmuir* 14, 1250–1255. https://doi.org/10.1021/la970354c

Hegler, F., Posth, N.R., Jiang, J., Kappler, A. (2008) Physiology of phototrophic iron(II)-oxidizing bacteria: implications for modern and ancient environments. *FEMS Microbiology Ecology* 66, 250–260. https://doi.org/10.1111/j.1574-6941.2008.00592.x

Hiemstra, T. (2013) Surface and mineral structure of ferrihydrite. *Geochimica et Cosmochimica Acta* 105, 316–325. https://doi.org/10.1016/j.gca.2012.12.002

Kim, M.-S., Lee, Y.-J. (2010) Optimization of culture conditions and electricity generation using *Geobacter sulfurreducens* in a dual-chambered microbial fuel-cell. *International Journal of Hydrogen Energy* 35, 13028–13034. https://doi.org/10.1016/j.ijhydene.2010.04.061

Kraal, P., van Genuchten, C.M., Behrends, T. (2022) Phosphate coprecipitation affects reactivity of iron (oxyhydr)oxides towards dissolved iron and sulfide. *Geochimica et Cosmochimica Acta* 321, 311–328. https://doi.org/10.1016/j.gca.2021.12.032

Lagarec, K., Rancourt, D.G. (1997) Extended Voigt-based analytic lineshape method for determining *N*-dimensional correlated hyperfine parameter distributions in Mössbauer spectroscopy. *Nuclear Instruments and Methods in Physics Research, Section B: Beam Interactions with Materials and Atoms* 129, 266–280. https://doi.org/10.1016/S0168-583X(97)00284-X

Lennie, A.R., Redfern, S.A.T., Schofield, P.F., Vaughan, D.J. (1995) Synthesis and Rietveld crystal structure refinement of mackinawite, tetragonal FeS. *Mineralogical Magazine* 59, 677–683. https://doi.org/10.1180/minmag.1995.059.397.10

Mansor, M., Fantle, M.S. (2019) A novel framework for interpreting pyrite-based Fe isotope records of the past. *Geochimica et Cosmochimica Acta* 253, 39–62. https://doi.org/10.1016/j.gca.2019.03.017

Mattievich, E., Danon, J. (1977) Hydrothermal synthesis and Mössbauer studies of ferrous phosphates of the homologous series $Fe_3^{2+}(PO_4)_2(H_2O)_n$. *Journal of Inorganic and Nuclear Chemistry* 39, 569–580. https://doi.org/10.1016/0022-1902(77)80567-8

Murad, E., Cashion, J. (2004) *Mössbauer Spectroscopy of Environmental Materials and Their Industrial Utilization*. First Edition, Springer, New York, NY. https://doi.org/10.1007/978-1-4419-9040-2

Murphy, J., Riley, J.P. (1962) A modified single solution method for the determination of phosphate in natural waters. *Analytica Chimica Acta* 27, 31–36. https://doi.org/10.1016/S0003-2670(00)88444-5

Nims, C., Cron, B., Wetherington, M., Macalady, J., Cosmidis, J. (2019) Low frequency Raman Spectroscopy for micron-scale and *in vivo* characterization of elemental sulfur in microbial samples. *Scientific Reports* 9, 7971. https://doi.org/10.1038/s41598-019-44353-6

Notini, L., Latta, D.E., Neumann, A., Pearce, C.I., Sassi, M., N'Diaye, A.T., Rosso, K.M., Scherer, M.M. (2019) A Closer Look at Fe(II) Passivation of Goethite. *ACS Earth and Space Chemistry* 3, 2717–2725. https://doi.org/10.1021/acsearthspacechem.9b00224

Peiffer, S., Behrends, T., Hellige, K., Larese-Casanova, P., Wan, M., Pollok, K. (2015) Pyrite formation and mineral transformation pathways upon sulfidation of ferric hydroxides depend on mineral type and sulfide concentration. *Chemical Geology* 400, 44–55. https://doi.org/10.1016/j.chemgeo.2015.01.023

Poulton, S.W. (2003) Sulfide oxidation and iron dissolution kinetics during the reaction of dissolved sulfide with ferrihydrite. *Chemical Geology* 202, 79–94. https://doi.org/10.1016/S0009-2541(03)00237-7

Raiswell, R., Canfield, D.E. (1998) Sources of iron for pyrite formation in marine sediments. *American Journal of Science* 298, 219–245. https://doi.org/10.2475/ajs.298.3.219

Rickard, D. (2019) How long does it take a pyrite framboid to form? *Earth and Planetary Science Letters* 513, 64–68. https://doi.org/10.1016/j.epsl.2019.02.019

Rickard, D., Luther, G.W. (2007) Chemistry of Iron Sulfides. *Chemical Reviews* 107, 514–562. https://doi.org/10.1021/cr0503658

Rickard, D., Butler, I.B., Oldroyd, A. (2001) A novel iron sulphide mineral switch and its implications for Earth and planetary science. *Earth and Planetary Science Letters* 189, 85–91. https://doi.org/10.1016/S0012-821X(01)00352-1

Rickard, D., Griffith, A., Oldroyd, A., Butler, I.B., Lopez-Capel, E., Manning, D.A.C., Apperley, D.C. (2006) The composition of nanoparticulate mackinawite, tetragonal iron(II) monosulfide. *Chemical Geology* 235, 286–298. https://doi.org/10.1016/j.chemgeo.2006.07.004

Roberts, A.P., Chang, L., Rowan, C.J., Horng, C.-S., Florindo, F. (2011) Magnetic properties of sedimentary greigite (Fe_3S_4): An update. *Reviews of Geophysics* 49, RG1002. https://doi.org/10.1029/2010RG000336

Schröder, C., Wan, M., Butler, I.B., Tait, A., Peiffer, S., McCammon, C.A. (2020) Identification of Mackinawite and Constraints on Its Electronic Configuration Using Mössbauer Spectroscopy. *Minerals* 10, 1090. https://doi.org/10.3390/min10121090

Straub, K.L., Hanzlik, M., Buchholz-Cleven, B.E.E. (1998) The Use of Biologically Produced Ferrihydrite for the Isolation of Novel Iron-Reducing Bacteria. *Systematic and Applied Microbiology* 21, 442–449. https://doi.org/10.1016/S0723-2020(98)80054-4

Sung, Y., Fletcher, K.E., Ritalahti, K.M., Apkarian, R.P., Ramos-Hernández, N., Sanford, R.A., Mesbah, N.M., Löffler, F.E. (2006) *Geobacter lovleyi* sp. nov. Strain SZ, a Novel Metal-Reducing and Tetrachloroethene-Dechlorinating Bacterium. *Applied and Environmental Microbiology* 72, 2775–2782. https://doi.org/10.1128/AEM.72.4.2775-2782.2006

Thiel, J., Byrne, J.M., Kappler, A., Schink, B., Pester, M. (2019) Pyrite formation from FeS and H_2S is mediated through microbial redox activity. *Proceedings of the National Academy of Sciences* 116, 6897–6902. https://doi.org/10.1073/pnas.1814412116

Tomaszewski, E.J., Olson, L., Obst, M., Byrne, J.M., Kappler, A., Muehe, E.M. (2020) Complexation by cysteine and iron mineral adsorption limit cadmium mobility during metabolic activity of *Geobacter sulfurreducens*. *Environmental Science: Processes and Impacts* 22, 1877–1887. https://doi.org/10.1039/D0EM00244E

Troelsen, H., Jørgensen, B.B. (1982) Seasonal dynamics of elemental sulfur in two coastal sediments. *Estuarine, Coastal and Shelf Sciene* 15, 255–266. https://doi.org/10.1016/0272-7714(82)90062-2

USGS (1985) Sulfide, titrimetric, iodometric. In: Fishman, M.J., Friedman, L.C. (Eds.) *Methods for determination of inorganic substances in water and fluvial sediments*. USGS Open-File Report 85-495, US Geological Survey, Denver, CO. https://doi.org/10.3133/ofr85495

van Gemerden, H., Tughan, C.S., de Wit, R., Herbert, R.A. (1989) Laminated microbial ecosystems on sheltered beaches in Scapa Flow, Orkney Islands. *FEMS Microbiology Ecology* 5, 87–101. https://doi.org/10.1111/j.1574-6968.1989.tb03661.x

Vandenberghe, R.E., de Grave, E., de Bakker, P.M.A., Krs, M., Hus, J.J. (1992) Mössbauer effect study of natural greigite. *Hyperfine Interactions* 68, 319–322. https://doi.org/10.1007/BF02396500

Wan, M., Schröder, C., Peiffer, S. (2017) Fe(III):S(-II) concentration ratio controls the pathway and the kinetics of pyrite formation during sulfidation of ferric hydroxides. *Geochimica et Cosmochimica Acta* 217, 334–348. https://doi.org/10.1016/j.gca.2017.08.036

Wang, W., Song, Y., Wang, X., Yang, Y., Liu, X. (2015) Alpha-Oxo Acids Assisted Transformation of FeS to Fe_3S_4 at Low Temperature: Implications for Abiotic, Biotic, and Prebiotic Mineralization. *Astrobiology* 15, 1043–1051. https://doi.org/10.1089/ast.2015.1373

Wilfert, P., Mandalidis, A., Dugulan, A.I., Goubitz, K., Korving, L., Temmink, H., Witkamp, G.J., Van Loosdrecht, M.C.M. (2016) Vivianite as an important iron phosphate precipitate in sewage treatment plants. *Water Research* 104, 449–460. https://doi.org/10.1016/j.watres.2016.08.032

Ye, L., Jing, C. (2022) Iron(III) reducing bacteria immobilise antimonite by respiring elemental sulfur. *Geochemical Perspectives Letters* 21, 37–41. https://doi.org/10.7185/geochemlet.2215

Zhu, F., Huang, Y., Ni, H., Tang, J., Zhu, Q., Long, Z., Zou, L. (2022) Biogenic iron sulfide functioning as electron-mediating interface to accelerate dissimilatory ferrihydrite reduction by *Shewanella oneidensis* MR-1. *Chemosphere* 288, 132661. https://doi.org/10.1016/j.chemosphere.2021.132661

Zopfi, J., Ferdelman, T.G., Fossing, H. (2004) Distribution and fate of sulfur intermediates—sulfite, tetrathionate, thiosulfate, and elemental sulfur—in marine sediments. In: Amend, J.P., Edwards, K.J., Lyons, T.W. (Eds.) *Sulfur Biogeochemistry - Past and Present*. GSA Special Papers, 379, Geological Society of America, Boulder, CO, 97–116. https://doi.org/10.1130/0-8137-2379-5.97